Image-guided wavefield tomography for VTI media

Vladimir Li[1], Antoine Guitton[1,2], Ilya Tsvankin[1], and Tariq Alkhalifah[1,3]
[1]*Center for Wave Phenomena, Colorado School of Mines*
[2]*DownUnder GeoSolutions*
[3]*King Abdullah University of Science and Technology*

ABSTRACT
Processing algorithms for transversely isotropic (TI) media are widely used in depth imaging and typically bring substantial improvements in reflector focusing and positioning. Here, we develop acoustic image-domain tomography (IDT) for reconstructing VTI (TI with a vertical symmetry axis) models from P-wave reflection data. The modeling operator yields an integral wave-equation solution, which is based on a separable dispersion relation and contains only P-waves. The zero-dip NMO velocity ($V_{\rm nmo}$) and anellipticity parameter η are updated by focusing energy in space-lag images obtained by least-squares reverse time migration (LSRTM). Application of LSRTM helps suppress aperture- and illumination-induced artifacts in space-lag gathers and improve the robustness of η-estimation. The trade-off between $V_{\rm nmo}$ and η is mitigated by a three-stage inversion algorithm that gradually relaxes the constraints on the spatial variation of η. Assuming that the depth profile of the Thomsen parameter δ is known at two or more borehole locations, we employ image-guided interpolation to constrain the depth scale of the parameter fields and the migrated image. Image-guided smoothing is also applied to the IDT gradients to facilitate convergence towards geologically plausible models. The algorithm is tested on synthetic reflection and borehole data from the structurally complicated elastic VTI Marmousi-II model. Although the initial velocity field is purely isotropic and substantially distorted, all three relevant parameters ($V_{\rm nmo}$, η, and δ) are estimated with sufficient accuracy. The algorithm is also applied to a line from a 3D ocean-bottom-node data set acquired in the Gulf of Mexico.

Key words: VTI, extended LSRTM, nonstationary filters, image-domain tomography, multiparameter inversion, image-guided

1 INTRODUCTION

Reflection tomography, routinely used in prestack depth imaging, reconstructs the background velocity model by iteratively improving the consistency of migrated images. Whereas tomography conventionally operates with ray-based imaging algorithms (e.g., Kirchhoff migration), reverse time migration (RTM) is better suited for complex geologic models. Wavefield-based methods often employ an extended imaging condition to evaluate angle-dependent illumination (Rickett and Sava, 2002; Sava and Fomel, 2003). Estimation of residual energy at nonzero lags helps update the velocity model, which is commonly done using differential semblance optimization (DSO) or image-power operators (Symes and Carazzone, 1991; Zhang and Shan, 2013).

However, application of image-domain tomography (IDT) remains limited, primarily because extended images contain residual energy induced by not only velocity errors but also uneven illumination and insufficient acquisition aperture (Mulder, 2014; Dafni and Symes, 2016). As a result, velocity updates generated by the DSO operator are susceptible to illumination-related contamination. This issue is particularly relevant for η-estimation because energy focusing in the extended domain is less sensitive to this parameter compared to $V_{\rm nmo}$ (Sava and Alkhalifah, 2012; V. Li et al., 2016). Thus, robust η-inversion with IDT requires suppressing illumination and aperture-truncation artifacts in extended images (V. Li et al., 2017).

IDT algorithms can be improved by using a better designed penalty operator (Yang and Sava, 2015) or a more robust imaging condition (Lameloise et al., 2015; Hou and Symes, 2017; Chauris and Cocher, 2017). Illumination issues can also be mitigated with least-squares RTM (LSRTM), as done in migration-based traveltime tomography (MBTT) (Clément et al., 2001) and reflection waveform inversion (Hicks and Pratt, 2001; Pattnaik et al., 2016). In this paper,

we employ LSRTM supplemented by nonstationary matching filters for gradient preconditioning (Guitton, 2017).

P-wave kinematics in VTI media is governed by the Thomsen parameters V_{P0} (vertical velocity), ϵ, and δ or by $V_{\rm nmo}$, η, and δ (Tsvankin, 2012). Because δ is poorly constrained by P-wave reflection moveout, robust VTI IDT algorithms require additional information typically provided by borehole data, such as check shots (Wang and Tsvankin, 2013a). Y. Li et al. (2016) augment the DSO and image-power terms in the objective function with petrophysical constraints. Knowledge of the covariance between the model parameters mitigates parameter trade-offs but the results indicate that realistic errors in the covariance matrix may lead to insufficient model updates.

As demonstrated by Wang and Tsvankin (2013b), trade-offs between the parameters of tilted TI media in ray-based reflection tomography can be reduced by using a multistage inversion scheme that gradually relaxes spatial constraints on the anisotropy coefficients. Pattnaik et al. (2016) employ a similar approach in RWI to resolve the parameters $V_{\rm nmo}$ and η. Velocity model-building can also benefit from image-guided constraints (Hale, 2009a; Ma et al., 2012; Guitton et al., 2012). In particular, image-guided smoothing of the anisotropy coefficients (Wang and Tsvankin, 2013a; Y. Li et al., 2016) helps steer the inversion for TI media toward geologically plausible solutions.

Here, we propose a nested image-domain optimization algorithm for estimating the VTI parameters $V_{\rm nmo}$, η, and δ. Whereas updates in $V_{\rm nmo}$ and η are driven by IDT (V. Li et al., 2017), the δ-field is obtained from image-guided interpolation between boreholes. Similarly to Wang and Tsvankin (2013a), we gradually relax image-guided smoothing constraints applied to the η-gradient.

We start by reviewing the wavefield extrapolation algorithm and application of nonstationary matching filters to LSRTM in TI media. Then we discuss the IDT objective functions and describe a three-stage inversion algorithm designed to stabilize η-estimation. Next, matching filters are applied to extended RTM gathers for a simple layered VTI model. The results demostrate that these filters efficiently suppress illumination-induced artifacts in the extended domain. Although the developed algorithm is acoustic, we test it on the reflection and borehole data generated for the elastic VTI Marmousi-II model. Finally, processing of a line from the 3D OBN data set acquired in the Gulf of Mexico demonstrates the feasibility of reconstructing the η-field using image-domain tomography.

2 METHODOLOGY

2.1 P-wave extrapolation operator in VTI media

Anisotropic wavefield extrapolation often employs the pseudoacoustic approximation (Alkhalifah, 1998, 2000), which can include different three-parameter sets (e.g., V_{P0}, ε, and δ or $V_{\rm nmo}$, η, and δ). Integral wave-equation solutions compute the phase shift for pure P-mode extrapolation (time-stepping) using the dispersion relation (Fomel et al., 2013b; Du et al., 2014). Following V. Li et al. (2017), we use the separable dispersion relation described in Schleicher and Costa (2015):

$$\omega^2 = (1+2\epsilon)V_{P0}^2\,k_x^2 + V_{P0}^2\,k_z^2 - 2(\epsilon-\delta)V_{P0}^2\,\frac{k_x^2\,k_z^2}{k_x^2+k_z^2} \times\left[1-2\epsilon\,\frac{k_x^2}{k_x^2+k_z^2}+2(\epsilon-\delta)\,\frac{k_x^2\,k_z^2}{(k_x^2+k_z^2)^2}\right], \quad (1)$$

where k_x and k_z are the horizontal and vertical wavenumbers. The Padé coefficients α and β are set to 1/2 and 1/4, respectively. The modeling operator for gradient computation is given in the weak-anellipticity (small η) approximation by:

$$\mathbf{L}_{\rm INT} = -\frac{\partial^2}{\partial t^2} - V_{\rm nmo}^2\,k_x^2 - \frac{V_{\rm nmo}^2}{1+2\delta}\,k_z^2 - 2\eta\,V_{\rm nmo}^2\frac{k_x^4}{k_x^2+k_z^2}. \quad (2)$$

The corresponding adjoint operator has the form (V. Li et al., 2017):

$$\mathbf{L}_{\rm INT}^{\dagger} = -\frac{\partial^2}{\partial t^2} - k_x^2 V_{\rm nmo}^2 - k_z^2\,\frac{V_{\rm nmo}^2}{1+2\delta} - \frac{2\,k_x^4}{k_x^2+k_z^2}\,\eta V_{\rm nmo}^2. \quad (3)$$

2.2 Extended least-squares RTM with matching filters

Information about angle-dependent subsurface illumination contained in extended images can be used for velocity model-building. The general imaging condition is formulated as (Sava and Vasconcelos, 2009):

$$I\left(\mathbf{x},\boldsymbol{\lambda},\tau\right) = \sum_{e,t} W_s\left(\mathbf{x}-\boldsymbol{\lambda},t-\tau\right) \times W_r\left(\mathbf{x}+\boldsymbol{\lambda},t+\tau\right), \quad (4)$$

where $I(\mathbf{x},\boldsymbol{\lambda},\tau)$ is the extended image, W_s and W_r denote the source and receiver wavefields, respectively, $\boldsymbol{\lambda}$ is the space lag, τ is the time lag, and e indicates summation over experiments (i.e., sources). Assuming perfect illumination and infinite bandwidth, imaging with the correct velocity model focuses events at zero lag. Therefore, energy defocusing in extended gathers provides information for velocity analysis.

However, algorithms designed to minimize residual energy in the extended domain must account for additional defocusing caused by uneven illumination and aperture truncation (Yang and Sava, 2015). Errors in the anisotropy coefficients often cause weaker defocusing compared to that due to velocity errors (V. Li et al., 2016). Thus, it is critically important for anisotropic IDT to suppress illumination-related artifacts before back-projecting image residuals, which can be achieved with nonstationary convolution filters. As shown by Guitton (2017), these filters provide a low-rank approximation to the true inverse Hessian and can be obtained as:

$$\mathbf{m}_0 = \mathbf{R}^{\rm T}(\mathbf{d_r},\mathbf{d_s}), \quad (5)$$

$$\mathbf{m}_1 = \mathbf{R}^{\rm T}\mathbf{R}\,\mathbf{m}_0, \quad (6)$$

$$\|\mathbf{m}_0 - \mathbf{B}\mathbf{m}_1\|^2 \approx 0, \quad (7)$$

where $\mathbf{m}_0$ is the RTM image, $\mathbf{R}^{\rm T}$ represents the sequence of

wavefield-extrapolation and extended-imaging operators, $\mathbf{d}_r$ are the recorded data, $\mathbf{d}_s$ is the source wavelet, $\mathbf{m}_1$ is the image obtained after demigration and migration (i.e., after the $\mathbf{R}^{\mathrm{T}}\mathbf{R}$ sequence), and $\mathbf{B}$ is the estimated nonstationary filter. Application of nonstationary matching filters involves the following steps:

- compute the "blurred" image by demigrating and migrating the RTM gathers (equation 6).
- estimate the "bank" of matching filters by solving equation 7 with the conjugate-gradient method.
- apply the filters $\mathbf{B}$ to the RTM image $\mathbf{m}_0$ to obtain the "pseudoinverse" image.

The matching filters computed with this approach substantially improve RTM extended gathers. Parameter estimation in structurally complex media can also benefit from applying this scheme to preconditioning of the LSRTM gradient (Guitton, 2017).

2.3 Objective function

Image-domain tomography is often based on residual-energy minimization with the DSO operator (Symes and Carazzone, 1991; Shen and Symes, 2008). An alternative approach is to maximize the zero-lag energy using the image-power (IP) criterion (Chavent and Jacewitz, 1995; Soubaras and Gratacos, 2007; Zhang and Shan, 2013). Robust VTI parameter estimation, however, is not feasible without additional constraints. Inversion driven by the DSO operator can produce significantly overestimated η-values, which "honor" the DSO criterion of small residuals. Whereas IP can update high model-wavenumber components, the corresponding objective function often has multiple local minima because the spatial positioning of such updates is controlled by the background velocity. The objective function can combine the DSO and IP criteria to increase the robustness of parameter estimation (Shan and Wang, 2013; Shan et al., 2014; Weibull and Arntsen, 2014; Y. Li et al., 2016):

$$\mathcal{J} = \mathcal{J}_{DSO} + \alpha\, \mathcal{J}_{IP}, \tag{8}$$

where α is a model-dependent weighting factor. The adjoint-state gradients of the terms $\mathcal{J}_{DSO}$ and $\mathcal{J}_{IP}$ for the wave-equation operator in equation 2 are derived in V. Li et al. (2017).

2.4 Multistage inversion algorithm

Below, we present a three-stage IDT algorithm designed to address the following issues that hamper VTI velocity analysis:

- simultaneous estimation of the parameters V_{nmo} and η is feasible only if the initial field of V_{nmo} (or V_{P0}) is sufficiently accurate.
- estimation of the parameter δ requires additional (e.g., borehole) information.
- high model-wavenumber components can be resolved only for accurate background velocity.

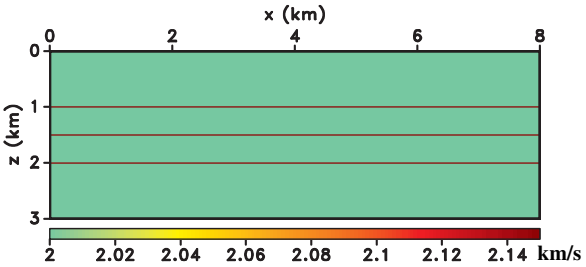

Figure 1. Constant-background VTI model with three horizontal perturbations in V_{nmo} at depths of 1, 1.5, and 2 km; η = 0.15, δ = 0.1. The wavefield is generated by 21 sources evenly spaced between 0 and 4 km; the maximum offset is 2 km.

After obtaining LSRTM gathers, the objective function is constructed using both the DSO and image-power terms (equation 8). It is convenient to invert for the dimensionless parameters $(V_{\mathrm{nmo}}/V_{\mathrm{nmo}}^{\mathrm{init}})^2$ ($V_{\mathrm{nmo}}^{\mathrm{init}}$ is the initial NMO velocity), $1+2\delta$, and $1+2\eta$, which are equal to unity for the initial isotropic model.

Whereas updates in V_{nmo} and η are driven by energy focusing in extended LSRTM gathers, the parameter δ is updated by image-guided interpolation between two (or more) boreholes, where the vertical δ-profile is assumed to be known. The interpolation is performed with the LSRTM image generated at the current iteration.

Similarly to Wang and Tsvankin (2013a), we design a three-stage inversion algorithm that gradually relaxes the constraints on the spatial variation of η. Because of the dominant influence of V_{nmo} on reflection moveout, errors in this parameter can bias the η-estimation. Therefore, we update V_{nmo} and η sequentially, as proposed by Pattnaik et al. (2016) for purposes of reflection waveform inversion. The first inversion stage is designed to update only V_{nmo}, whereas the second stage (when the V_{nmo}-field is more accurate) is limited to updating η. Finally, at the third stage V_{nmo} and η are updated simultaneously. The weighting factor α in equation 8 is fixed for each stage and increases during the optimization process to assign a larger weight to the IP term as the model becomes more accurate.

To steer the algorithm towards geologically plausible solutions, image-guided smoothing (Hale, 2009b) is applied to the V_{nmo}- and η-gradients (Guitton et al., 2012; Wang and Tsvankin, 2013a; Y. Li et al., 2016). Model updating is carried out by incorporating the gradients in the L-BFGS inversion algorithm (Nocedal and Wright, 2006).

3 HORIZONTALLY LAYERED MODEL

First, we demonstrate on a simple model that nonstationary matching filters are capable of suppressing illumination-related artifacts in extended images. The model includes three horizontal interfaces (formed by perturbations in V_{nmo}), which are embedded in a homogeneous VTI background (Figure 1). The wavefield is excited by 21 sources evenly spaced at the surface. Figure 2 shows space-lag CIGs computed for a dis-

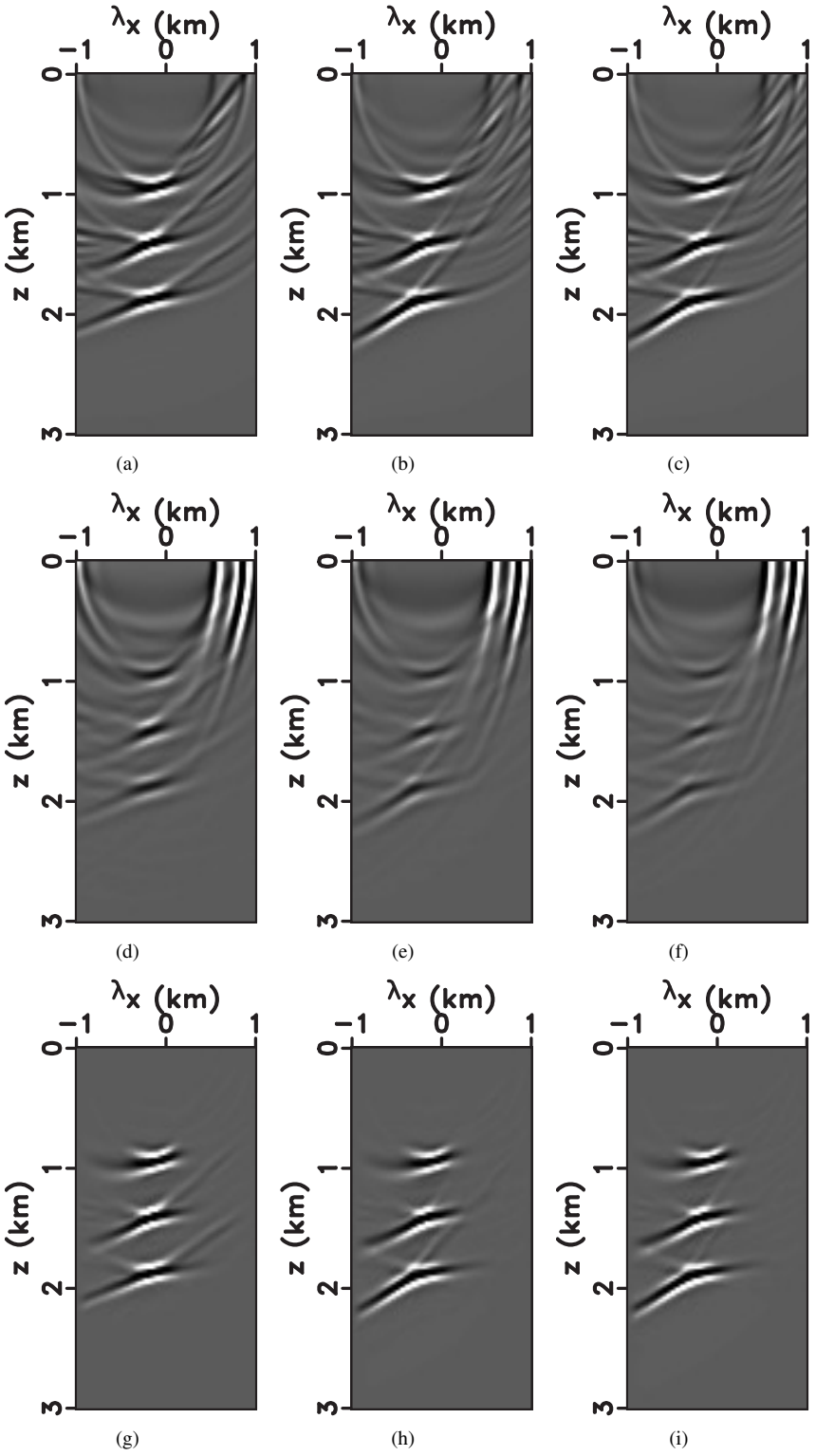

Figure 2. Extended images for the model in Figure 1 with η = 0 and $V_{\rm nmo}$ reduced by 10%. Each column corresponds to a different horizontal coordinate: (a,d,g) 1 km, (b,e,h) 2 km, and (c,f,i) 3 km. The top row (a-c) shows the cross-correlation RTM gathers, the second row (d-f) the gathers after demigration and migration, and the last row (g-i) the gathers after applying the matching filters.

torted model, in which η is set to zero (actual η = 0.15) and $V_{\rm nmo}$ is reduced by 10%. The CIGs contain three types of residual energy:

- the main energy-focusing point is shifted away from zero lag because of the error in $V_{\rm nmo}$.
- there is a "linear" energy defocusing caused by the distortion in η (V. Li et al., 2016; Sava and Alkhalifah, 2012).
- there are aperture-truncation artifacts which are most pronounced near the surface.

Defocusing due to aperture truncation is particularly visible in the "blurred" gathers obtained after applying the demigration and migration operators (Figure 2 d-f). The matching filters substantially suppress the aperture-truncation artifacts without distorting the "useful" residuals caused by the errors in $V_{\rm nmo}$ and η (Figure 2 g-i).

4 MARMOUSI MODEL

Next, we test the algorithm on the VTI Marmousi-II model shown in Figure 3 (Guitton and Alkhalifah, 2016). The data consist of 100 shot gathers produced with an elastic finite-difference operator. We use the "streamer" acquisition geometry with the maximum offset equal to 6 km. To constrain the depth scale of the model, the parameter δ is assumed to be known at two "borehole" locations (Figure 3a).

The initial model is isotropic and weakly laterally heterogeneous; it is obtained by applying strong smoothing to the actual $V_{\rm nmo}$-field (Figure 4). The extended RTM image computed with the initial model is significantly defocused due to velocity errors, as well as uneven illumination and aperture truncation (Figure 5). Two iterations of extended LSRTM substantially improve the image (Figure 6), which is then used in guided interpolation between the boreholes to obtain the initial δ-field. Imaging with the interpolated δ-field helps improve the spatial positioning of the migrated reflectors. Then the sequence of LSRTM and guided interpolation is applied for a second time to refine the spatial distribution of δ (Figure 7).

Estimation of the parameters $V_{\rm nmo}$ and η is carried out using the three-stage IDT algorithm described above. The inner loop of the algorithm includes two iterations of the preconditioned extended LSRTM. Whereas the parameters $V_{\rm nmo}$ and η are computed by back-projecting the image residuals, the δ-field is obtained from image-guided interpolation and kept fixed at each inversion stage.

Because the initial model is highly inaccurate, it is not feasible to estimate $V_{\rm nmo}$ and η simultaneously without improving the $V_{\rm nmo}$-field. In the shallow region, the overestimated $V_{\rm nmo}$ produces negative updates in η, thus moving the parameter search in the wrong direction. Therefore, at the first inversion stage, we update only $V_{\rm nmo}$ and set the factor α in the objective function (equation 8) to 0.5, which assigns a larger weight to the DSO term. After two model updates, the $V_{\rm nmo}$ -field is sufficiently improved (Figure 8) to focus energy in extended gathers closer to zero lag (Figure 9) and make η-estimation possible.

The second inversion stage is designed to update only η using the elliptic (η = 0) velocity model obtained after stage 1. The factor α in equation 8 is set to unity to assign equal weights to both objective-function terms, which helps stabilize η-updates. To increase the robustness of η-estimation, strong image-guided smoothing is applied to the η-gradient.

After two iterations, the algorithm does not refine η anymore. The higher accuracy of the updated η-field (Figure 10) improves event focusing in extended gathers (Figure 11). Image-guided smoothing is instrumental in resolving the strongly anisotropic layer to the left of the faulted area at a depth of 2 km. However, η remains largely unconstrained below 3 km, which is due to relatively small offset-to-depth ratios and increasing errors in the NMO velocity with depth.

With the more accurate $V_{\rm nmo}$- and η-fields, at the third inversion stage we update the two parameters simultaneously and also invert for higher model-wavenumber components. The factor α is set to two to emphasize the IP term in the objective function. We also relax the smoothing constraints but still apply stronger image-guided smoothing to the η-gradient compared to that for $V_{\rm nmo}$. This is justified by the fact that reflection data help reconstruct $V_{\rm nmo}$ with a higher spatial resolution than η. Two more model updates add higher-contrast features to the $V_{\rm nmo}$-field and slightly increase the resolution of η (Figure 12). These updates, however, provide only a marginal improvement in the focusing of the migrated events (Figure 13).

5 GULF OF MEXICO DATA SET

Here, we provide preliminary results for a line from a 3D ocean-bottom node (OBN) data set acquired in the Gulf of Mexico (courtesy of Shell). Preprocessing includes data projection onto the line, debubbling, P-Z summation, and normalization with a smooth data envelope that increases the amplitudes of reflections from the deeper layers. The elliptic (η = 0) initial model provided by Shell features a salt dome embedded in subhorizontal sediments (Figure 13). To increase the robustness of imaging and eliminate diffractions, we smooth the edges of the original salt body. Given the relative sparseness of OBN data, the mirror imaging technique (Figure 13a) is employed to increase the illumination. Following Guitton (2017), the matching filters are used to precondition the first two LSRTM iterations. Figure 14 shows the results after 16 iterations, which reduce the initial data misfit by 40%.

Because the initial model produces relatively weak defocusing in extended gathers, we start the inversion with stage 2 designed to update only η; the weighting factor α is set to unity. We do not make any updates in the δ-field provided by Shell. The sensitivity kernels of η mainly involve horizontal wavenumbers, so the summation of the η-gradients over individual shots mitigates the sparseness of the ocean-bottom nodes. Figure 15 shows the initial inversion gradients for η before (Figure 15a) and after (Figure 15b) preconditioning that includes image-guided smoothing and smooth-envelope normalization. We also set η to zero in the water and salt body, as well as at depths below 4 km where this parameter cannot be reliably constrained within the available range of offsets.

6 CONCLUSIONS

We presented an acoustic IDT algorithm designed to reconstruct P-wave VTI velocity models using wave-equation imaging. Application of LSRTM plays a crucial role in suppressing aperture- and illumination-induced artifacts in the extended domain. Nonstationary matching filters facilitate the convergence of LSRTM, which significantly improves the efficiency of the entire IDT algorithm. The three-stage inversion strategy mitigates the trade-off between the parameters $V_{\rm nmo}$ and η, and image-guided smoothing steers the algorithm towards geologically plausible solutions. The parameter δ is reconstructed from image-guided interpolation between available boreholes. The high computational cost of the inner-loop LSRTM is partly compensated by a small number of outer-loop iterations.

The algorithm was applied to the elastic VTI Marmousi-II model starting from a purely isotropic, substantially distorted velocity field. The updates in $V_{\rm nmo}$, η, and δ obtained after six iterations of IDT significantly improved the LSRTM image. Preliminary inversion results for a line from the Gulf of Mexico suggest that the initial elliptic model can be improved with positive η-updates. The robustness of field-data applications can be increased by extending the algorithm to 3D which, however, remains prohibitively expensive. Ongoing work includes an extension of the method to tilted TI media.

7 ACKNOWLEDGMENTS

This work was supported by the Consortium Project on Seismic Inverse Methods for Complex Structures at CWP and competitive research funding from King Abdullah University of Science and Technology (KAUST). We are grateful to Shell Exploration and Production Company for sharing the 3D Gulf of Mexico data set with Colorado School of Mines, and their permission to publish the results using this data set. We also thank Daniel Rocha (CWP) for help in preprocessing the data. The numeric examples in this paper are generated with the Madagascar open-source software package (Fomel et al., 2013a) freely available from http://www.ahay.org.

REFERENCES

Alkhalifah, T., 1998, Acoustic approximations for processing in transversely isotropic media: Geophysics, **63**, 623–631.

———, 2000, An acoustic wave equation for anisotropic media: Geophysics, **65**, 1239–1250.

Chauris, H., and E. Cocher, 2017, From migration to inversion velocity analysis: Geophysics, **82**, S207–S223.

Chavent, G., and C. A. Jacewitz, 1995, Determination of background velocities by multiple migration fitting: Geophysics, **60**, 476–490.

Clément, F., G. Chavent, and S. Gómez, 2001, Migrationbased traveltime waveform inversion of 2D simple structures: A synthetic example: Geophysics, **66**, 845–860.

Dafni, R., and W. W. Symes, 2016, Kinematic artifacts in the subsurface-offset extended image and their elimination by a dip-domain specularity filter: Geophysics, **81**, S477–S495.

Du, X., P. J. Fowler, and R. P. Fletcher, 2014, Recursive integral time-extrapolation methods for waves: A comparative review: Geophysics, **79**, T9–T26.

Fomel, S., P. Sava, I. Vlad, Y. Liu, and V. Bashkardin, 2013a, Madagascar: open-source software project for multidimensional data analysis and reproducible computational experiments: Journal of Open Research Software, **1(1)**, e8.

Fomel, S., L. Ying, and X. Song, 2013b, Seismic wave extrapolation using lowrank symbol approximation: Geophysical Prospecting, **61**, 526–536.

Guitton, A., 2017, Fast 3D least-squares RTM by preconditioning with nonstationary matching filters: SEG Technical Program Expanded Abstracts, 4395–4399.

Guitton, A., and T. Alkhalifah, 2016, An optimal parameterization for full waveform inversion in anisotropic media: 78th EAGE Conference and Exhibition.

Guitton, A., G. Ayeni, and E. Díaz, 2012, Constrained full-waveform inversion by model reparameterization: Geophysics, **77**, R117–R127.

Hale, D., 2009a, Imageguided blended neighbor interpolation of scattered data: SEG Technical Program Expanded Abstracts 2009, 1127–1131.

———, 2009b, Structure-oriented smoothing and semblance: CWP Project Review Report, 635, 1–10.

Hicks, G. J., and R. G. Pratt, 2001, Reflection waveform inversion using local descent methods: Estimating attenuation and velocity over a gassand deposit: Geophysics, **66**, 598–612.

Hou, J., and W. W. Symes, 2017, An alternative formula for approximate extended born inversion: Geophysics, **82**, S1–S8.

Lameloise, C.-A., H. Chauris, and M. Noble, 2015, Improving the gradient of the image-domain objective function using quantitative migration for a more robust migration velocity analysis: Geophysical Prospecting, **63**, 391–404.

Li, V., I. Tsvankin, and T. Alkhalifah, 2016, Analysis of RTM extended images for VTI media: Geophysics, **81**, S139–S150.

Li, V., H. Wang, I. Tsvankin, E. Díaz, and T. Alkhalifah, 2017, Inversion gradients for acoustic VTI wavefield tomography: Geophysics, **82**, WA55–WA65.

Li, Y., B. Biondi, R. Clapp, and D. Nichols, 2016, Integrated VTI model building with seismic data, geologic information, and rock-physics modeling part 1: Theory and synthetic test: Geophysics, **81**, C177–C191.

Ma, Y., D. Hale, B. Gong, and Z. J. Meng, 2012, Image-guided sparse-model full waveform inversion: Geophysics, **77**, R189–R198.

Mulder, W., 2014, Subsurface offset behaviour in velocity analysis with extended reflectivity images: Geophysical Prospecting, **62**, 17–33.

Nocedal, J., and S. J. Wright, 2006, Numerical optimization, 2 ed.: Springer-Verlag New York, Inc.

Pattnaik, S., I. Tsvankin, H. Wang, and T. Alkhalifah, 2016,

Full-waveform inversion with reflected waves for 2D VTI media: SEG Technical Program Expanded Abstracts, 413–418.

Rickett, J., and P. Sava, 2002, Offset and angle–domain common image-point gathers for shot-profile migration: Geophysics, **67**, 883–889.

Sava, P., and T. Alkhalifah, 2012, Anisotropy signature in extended images from reverse-time migration: SEG, Technical Program Expanded Abstracts, 1–6.

Sava, P., and S. Fomel, 2003, Angle-domain common-image gathers by wavefield continuation methods: Geophysics, **68**, 1065–1074.

Sava, P., and I. Vasconcelos, 2009, Efficient computation of extended images by wavefield-based migration: SEG, Technical Program Expanded Abstracts, 2824–2828.

Schleicher, J., and J. C. Costa, 2015, A separable strong-anisotropy approximation for pure qp wave propagation in TI media: SEG Technical Program Expanded Abstracts, 3565–3570.

Shan, G., and Y. Wang, 2013, Rtm based wave equation migration velocity analysis: SEG Technical Program Expanded Abstracts 2013, 4726–4731.

Shan, G., Y. Wang, and U. Albertin, 2014, Wave equation migration velocity analysis by wavefield decomposition: SEG Technical Program Expanded Abstracts, 4680–4685.

Shen, P., and W. W. Symes, 2008, Automatic velocity analysis via shot profile migration: Geophysics, **73**, VE49–VE59.

Soubaras, R., and B. Gratacos, 2007, Velocity model building by semblance maximization of modulated-shot gathers: Geophysics, **72**, U67–U73.

Symes, W. W., and J. J. Carazzone, 1991, Velocity inversion by differential semblance optimization: Geophysics, **56**, 654–663.

Tsvankin, I., 2012, Seismic signatures and analysis of reflection data in anisotropic media, third edition: Society of Exploration Geophysicists.

Wang, X., and I. Tsvankin, 2013a, Multiparameter TTI tomography of P-wave reflection and VSP data: Geophysics, **78**, WC51–WC63.

———, 2013b, Ray–based gridded tomography for tilted transversely isotropic media: Geophysics, **78**, C11–C23.

Weibull, W. W., and B. Arntsen, 2014, Anisotropic migration velocity analysis using reverse-time migration: Geophysics, **79**, R13–R25.

Yang, T., and P. Sava, 2015, Image-domain wavefield tomography with extended common-image-point gathers: Geophysical Prospecting, 1086–1096.

Zhang, Y., and G. Shan, 2013, Wave-equation migration velocity analysis using partial stack-power maximization: SEG Technical Program Expanded Abstracts, 4847–4852.

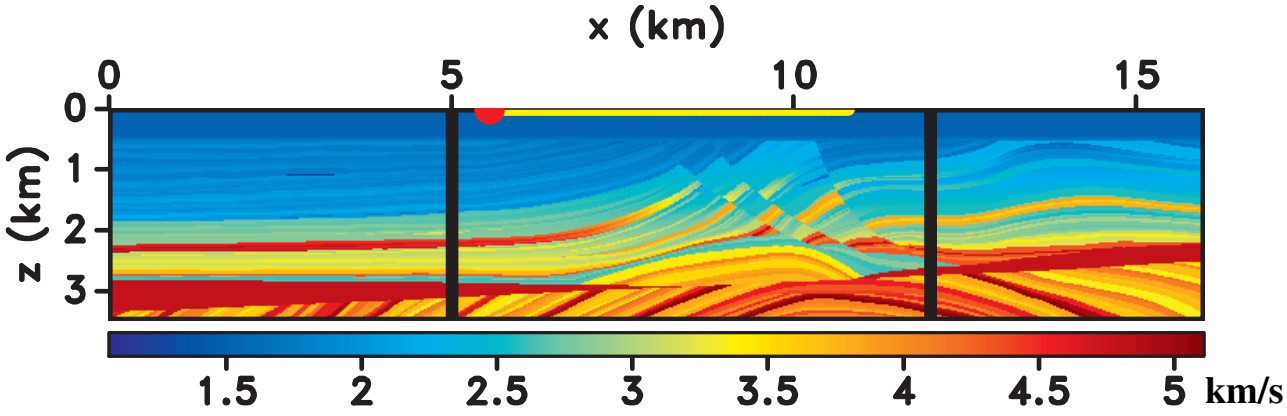

(a)

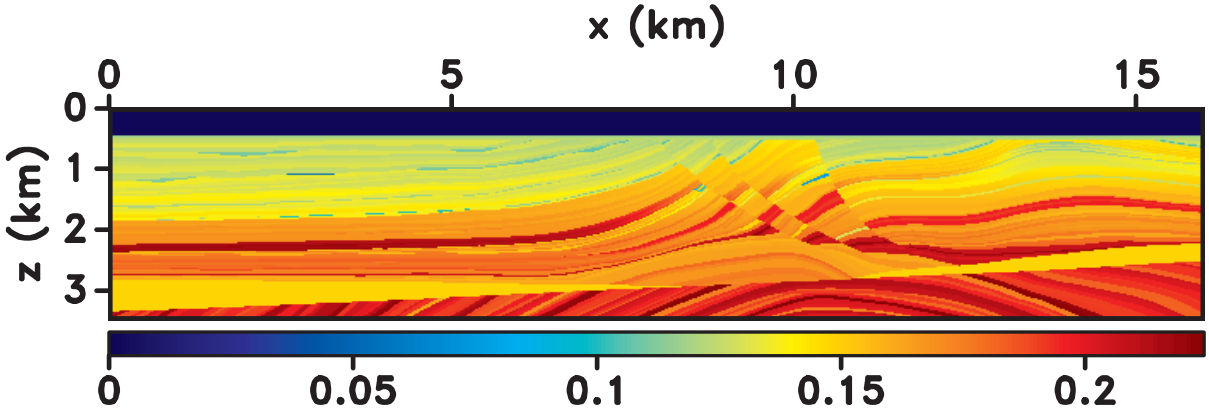

(b)

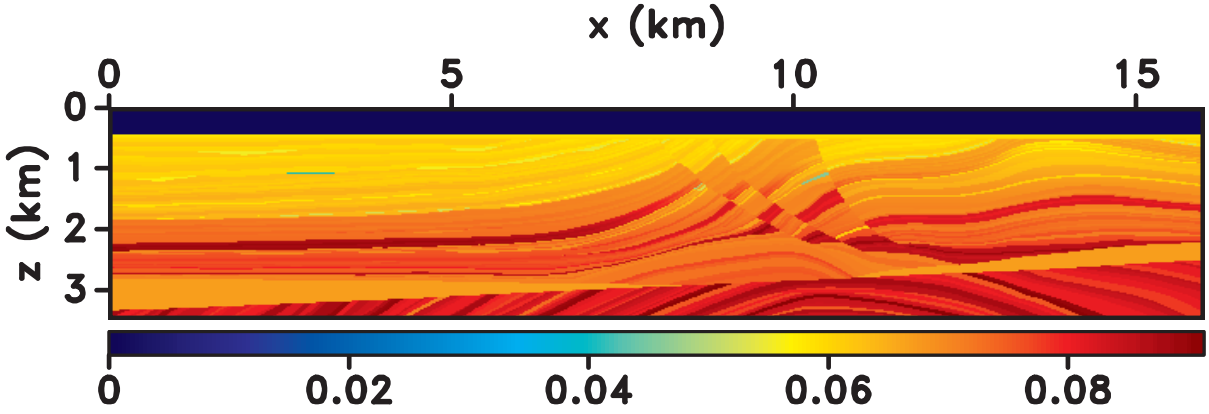

(c)

Figure 3. Parameters of the elastic VTI Marmousi-II model: (a) V_{nmo}, (b) η, and (c) δ. The vertical black lines on plot (a) mark the "borehole" locations where δ-profiles are available. 100 sources (one is marked by a red dot) are evenly spaced at the surface between 0 and 12 km. For each source location, the data are recorded by a "streamer" array (marked by a yellow line) with a maximum offset of 6 km.

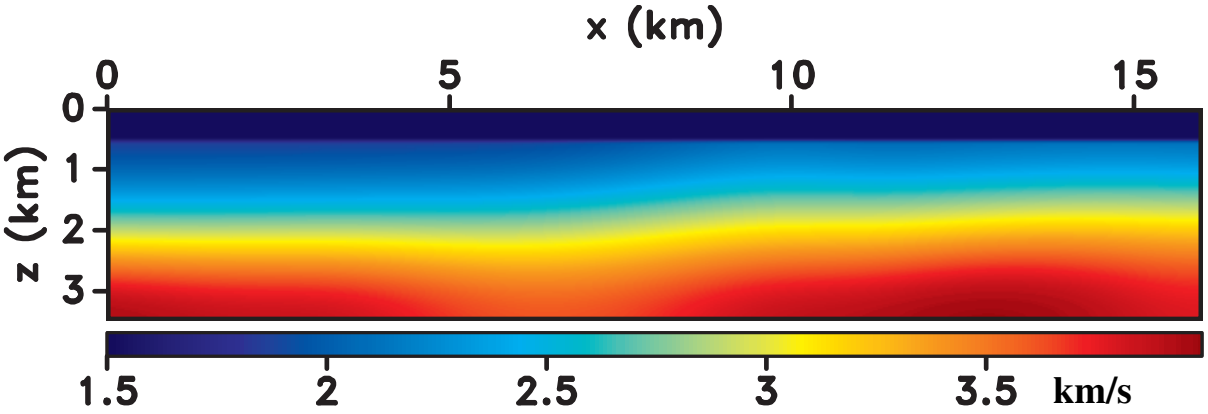

Figure 4. Initial isotropic velocity model obtained by smoothing the actual V_{nmo}-field.

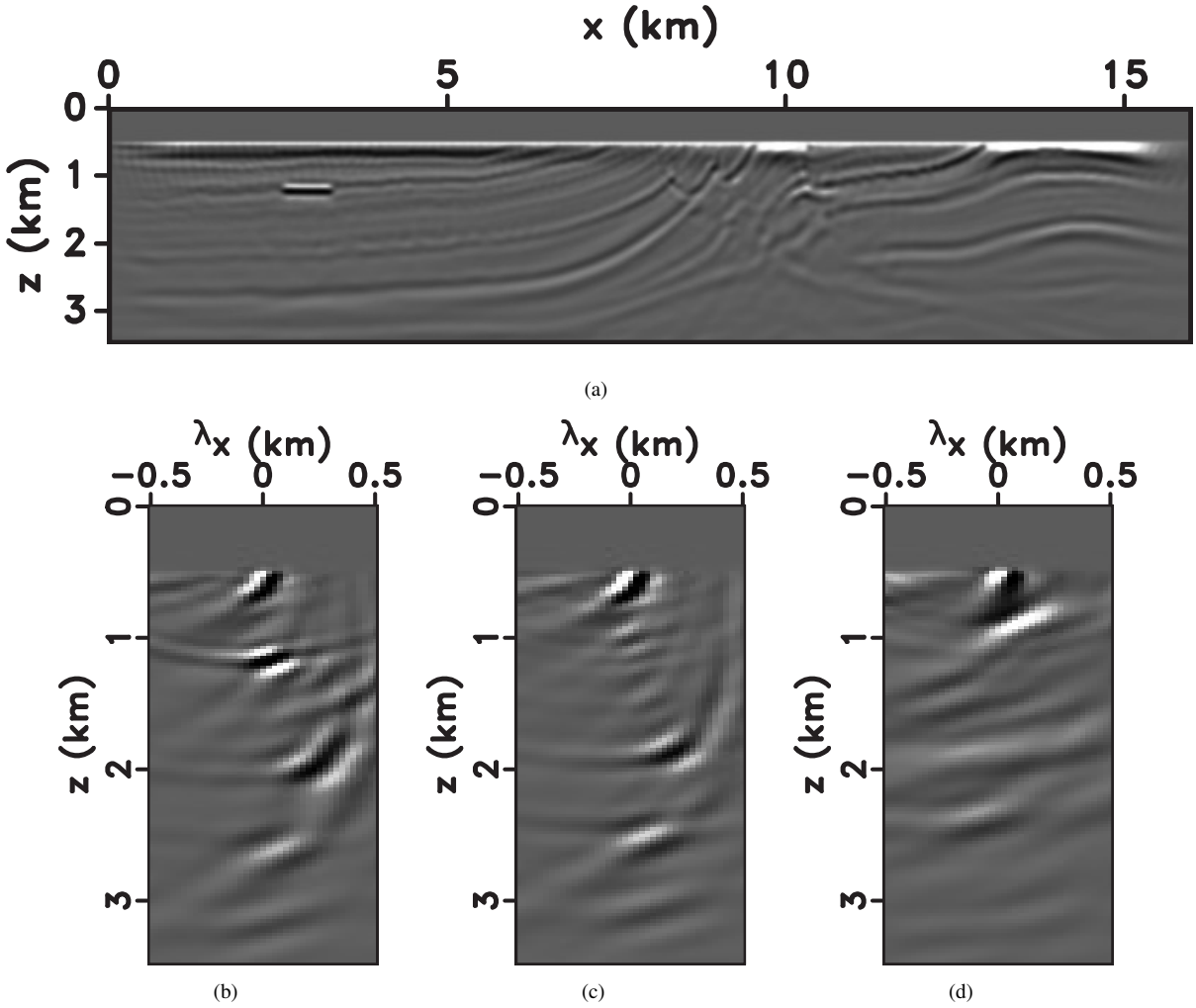

Figure 5. RTM output for the model from Figure 3 computed with the initial isotropic model. (a) The conventional image and (b-d) the space-lag gathers at (b) 3 km, (c) 5 km, and (d) 9 km.

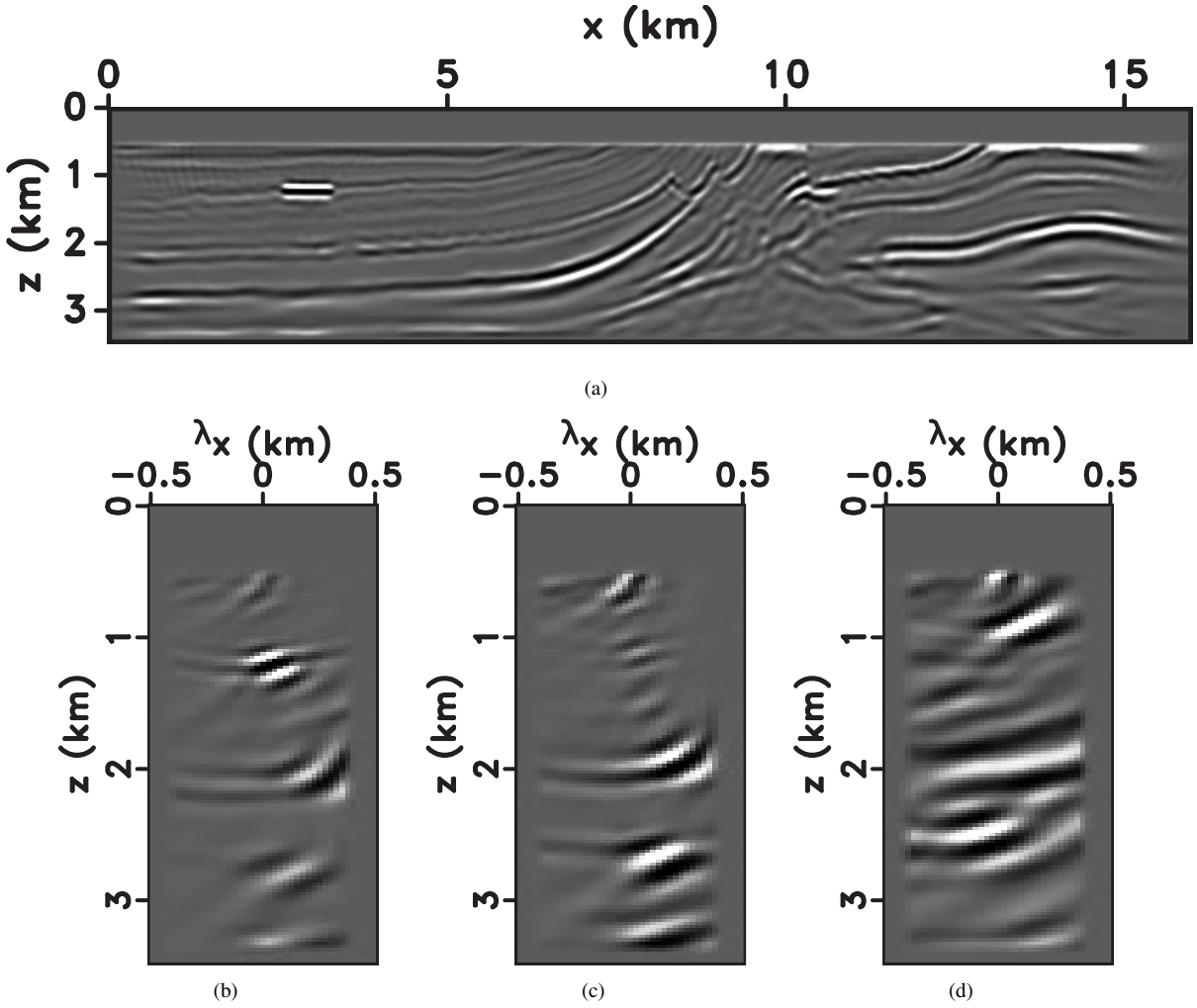

Figure 6. LSRTM output for the model from Figure 3 computed with the initial isotropic model. (a) The conventional image and (b-d) the space-lag gathers at (b) 3 km, (c) 5 km, and (d) 9 km.

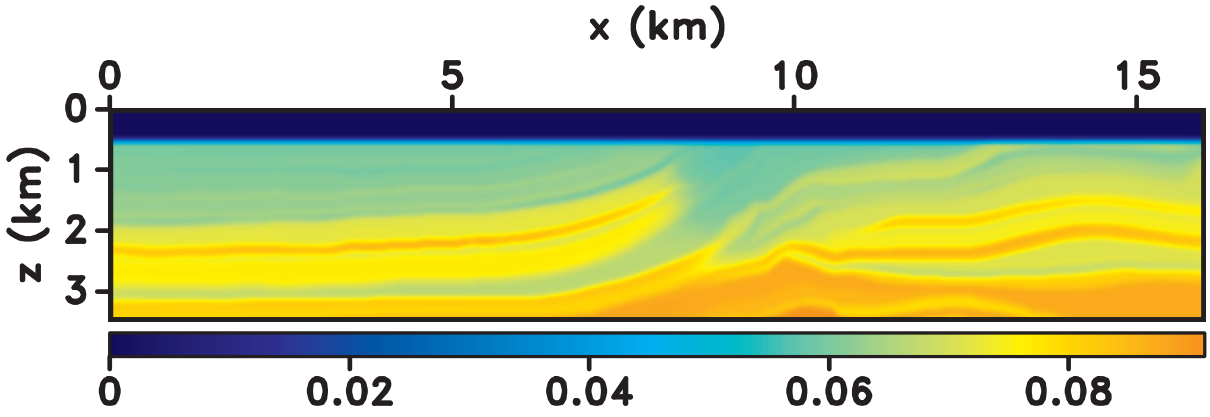

(a)

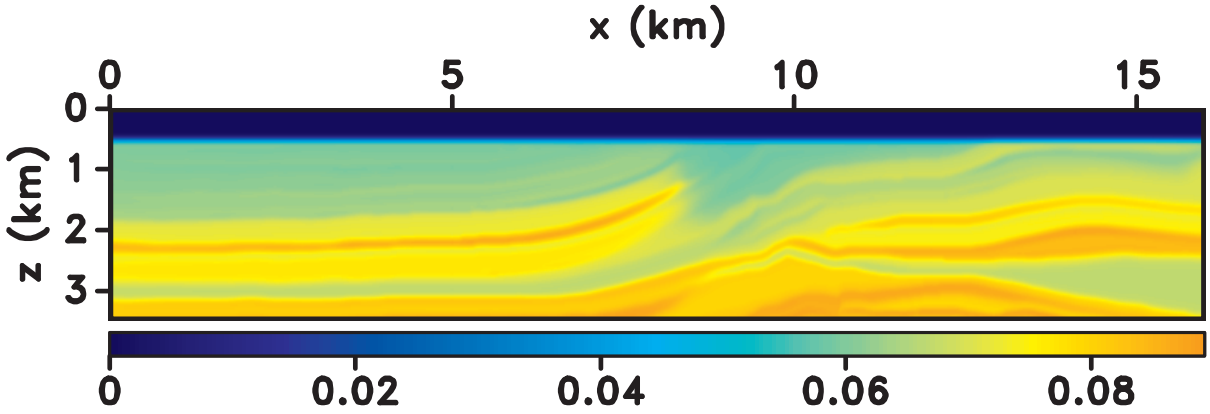

(b)

Figure 7. Initial δ-fields obtained by guided interpolation between the boreholes in Figure 3a using (a) the "purely isotropic" LSRTM image and (b) the refined image.

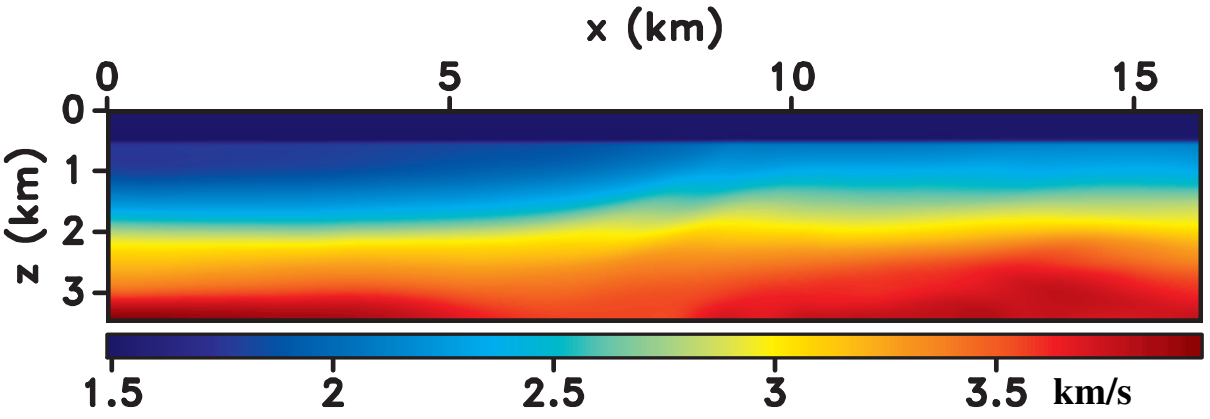

Figure 8. NMO velocity after stage 1 of the inversion.

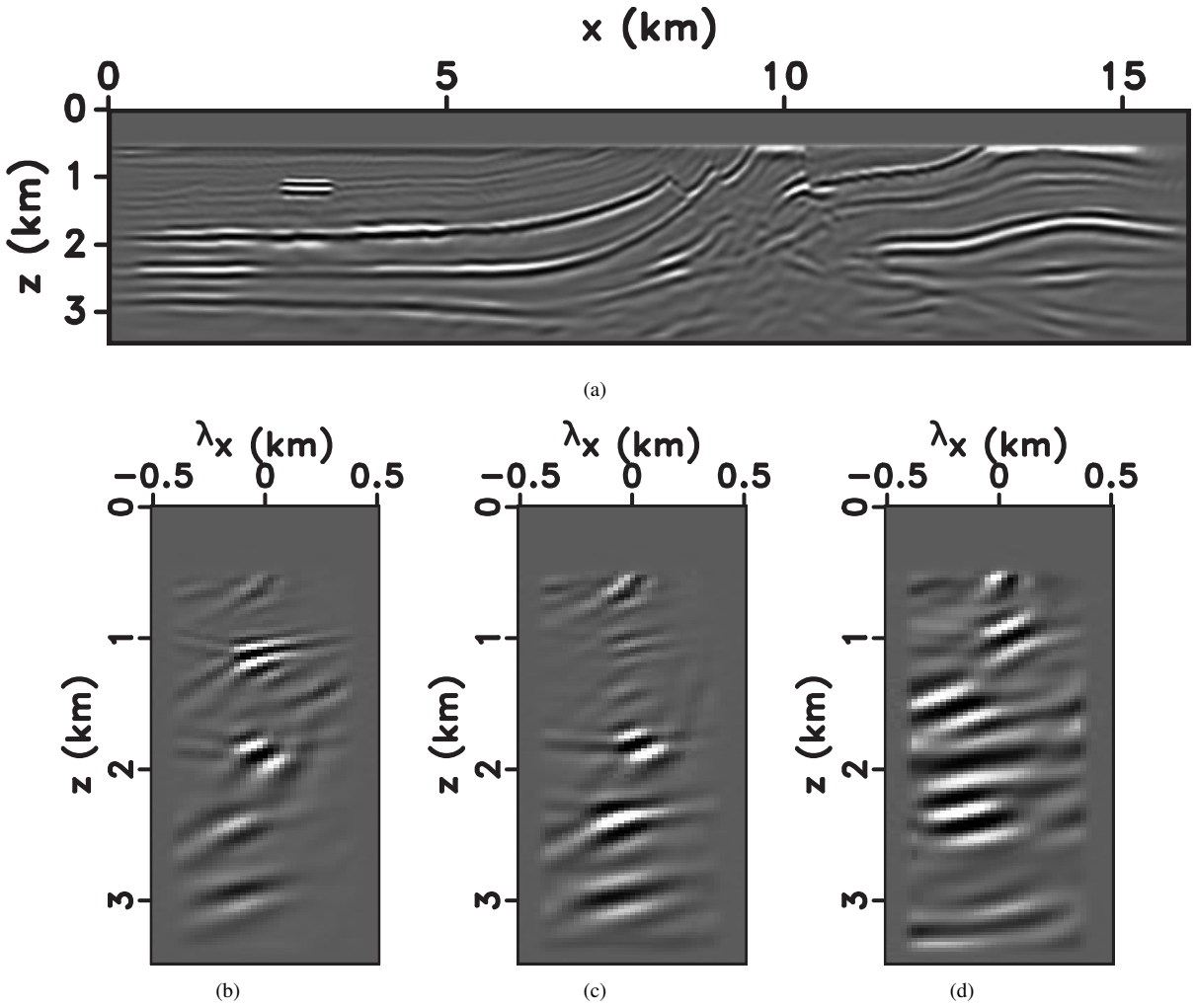

Figure 9. LSRTM output for the model from Figure 3 computed with the updated isotropic model. (a) The conventional image and (b-d) the space-lag gathers at (b) 3 km, (c) 5 km, and (d) 9 km.

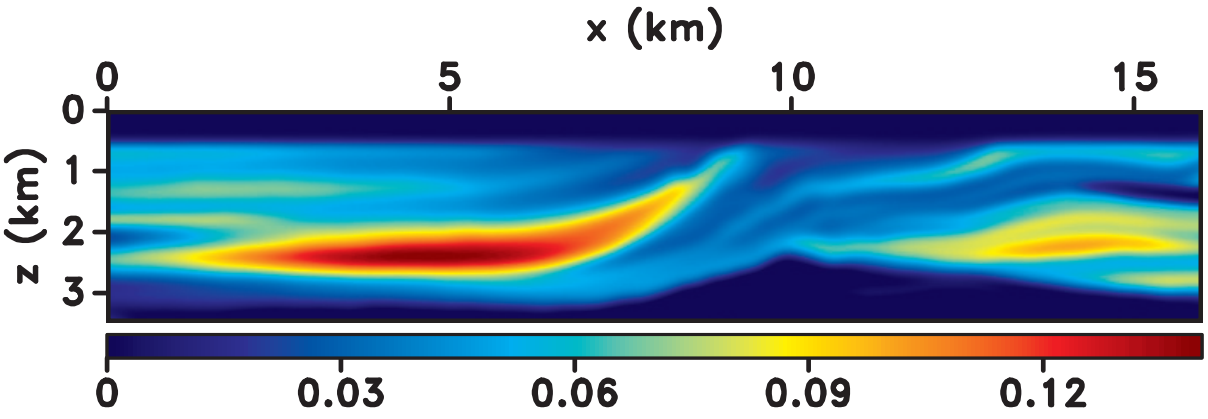

Figure 10. Parameter η after stage 2 of the inversion.

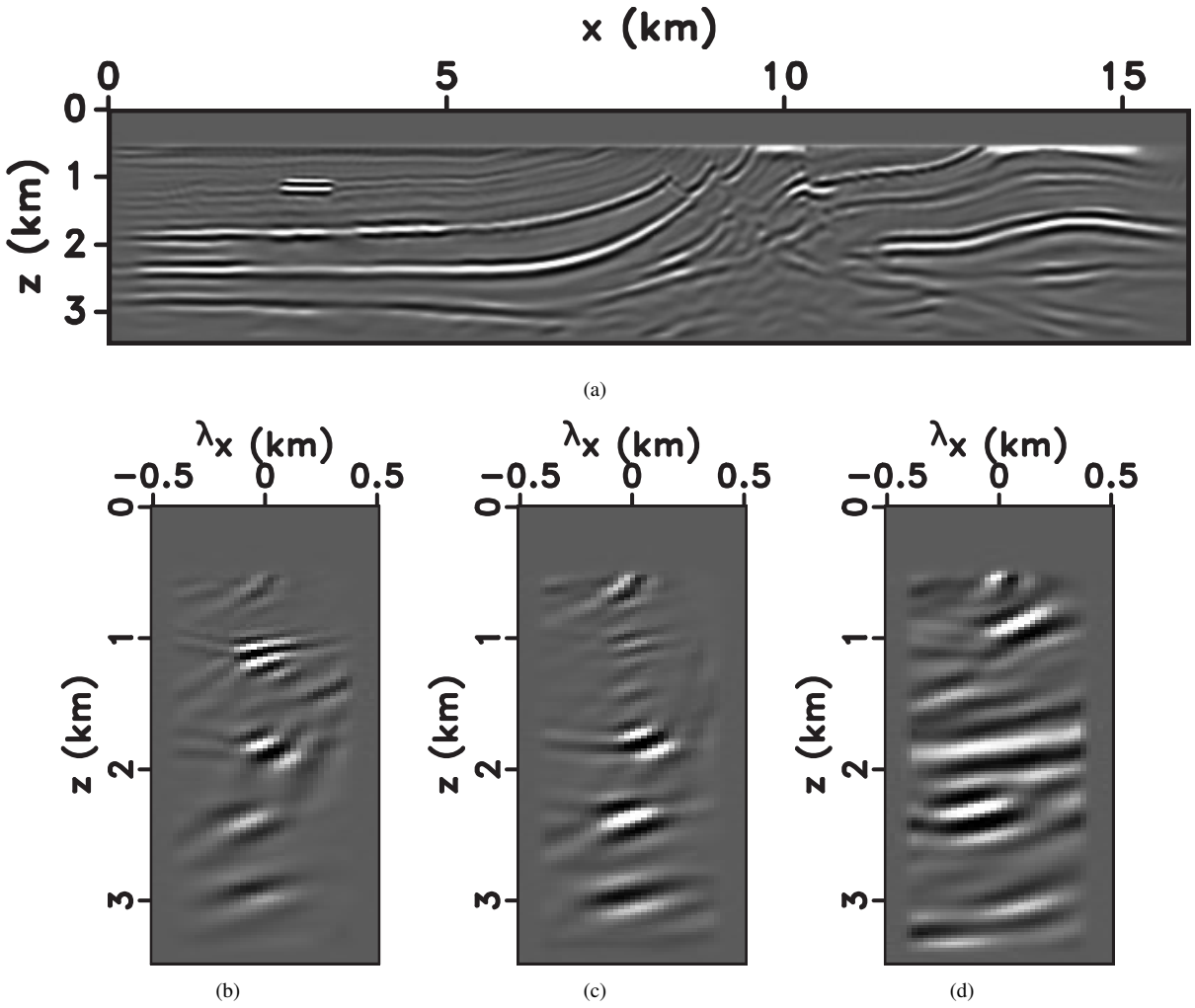

Figure 11. LSRTM output for the model from Figure 3 after stage 2. (a) The conventional image and (b-d) the space-lag gathers at (b) 3 km, (c) 5 km, and (d) 9 km.

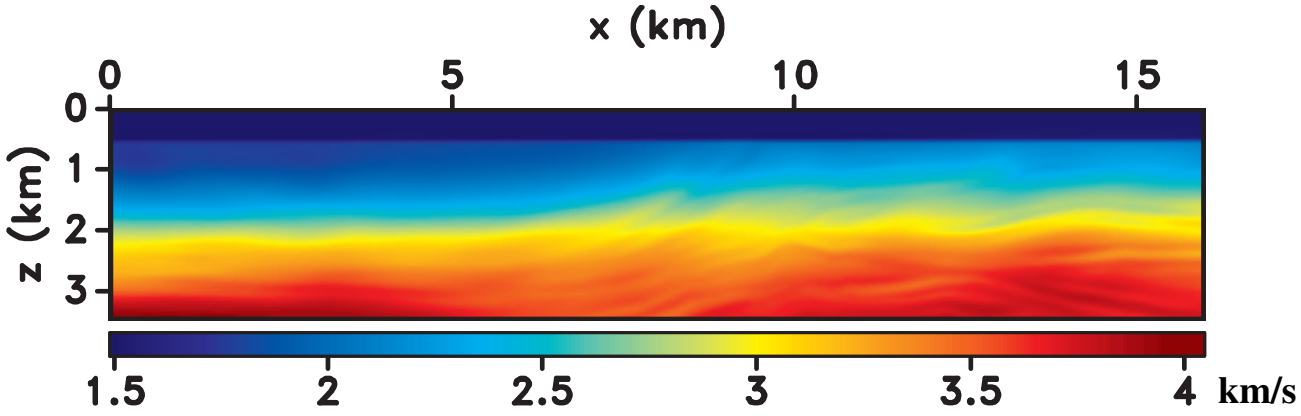

(a)

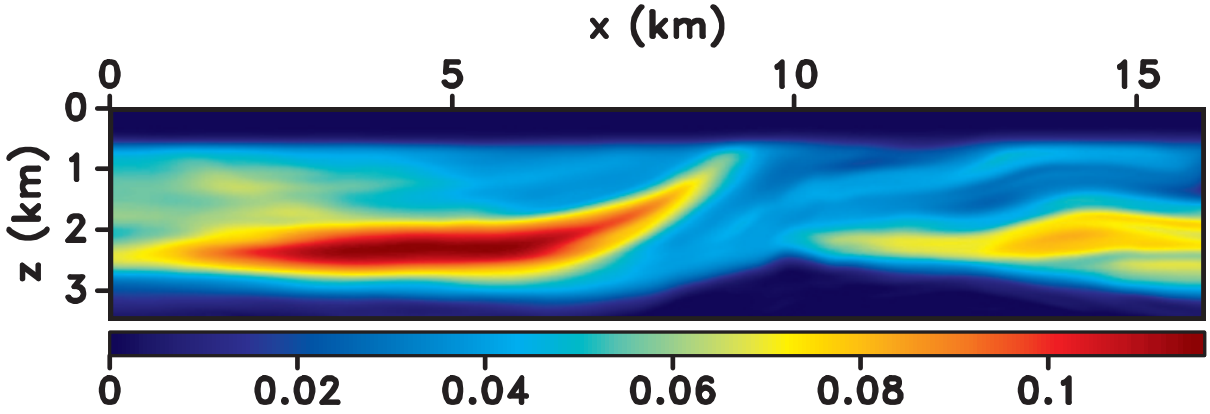

(b)

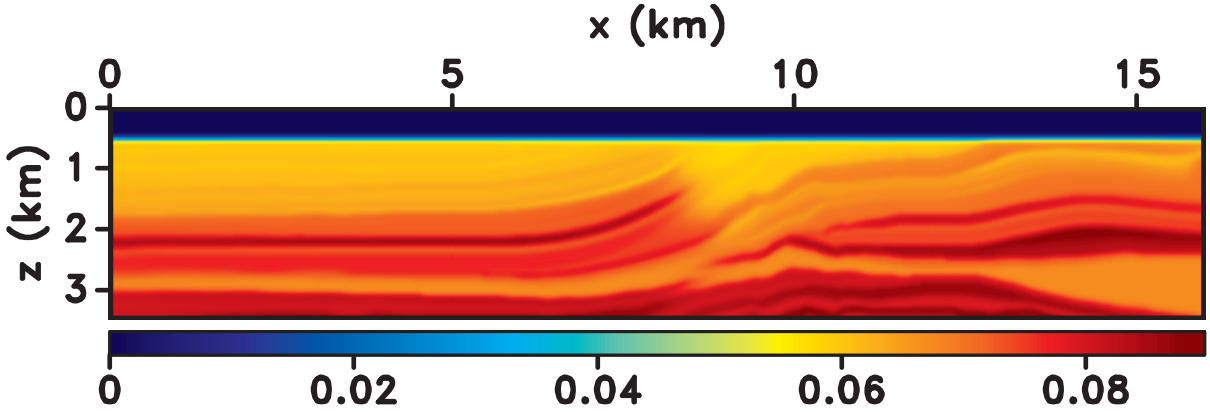

(c)

Figure 12. Inverted parameters for the model from Figure 3: (a) V_{nmo}, (b) η, and (c) δ.

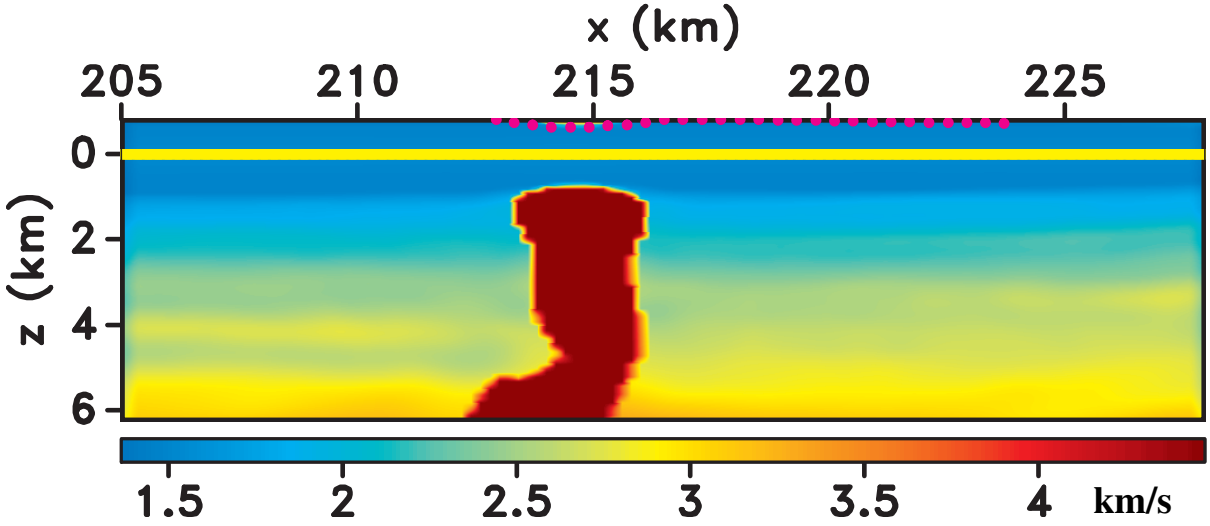

(a)

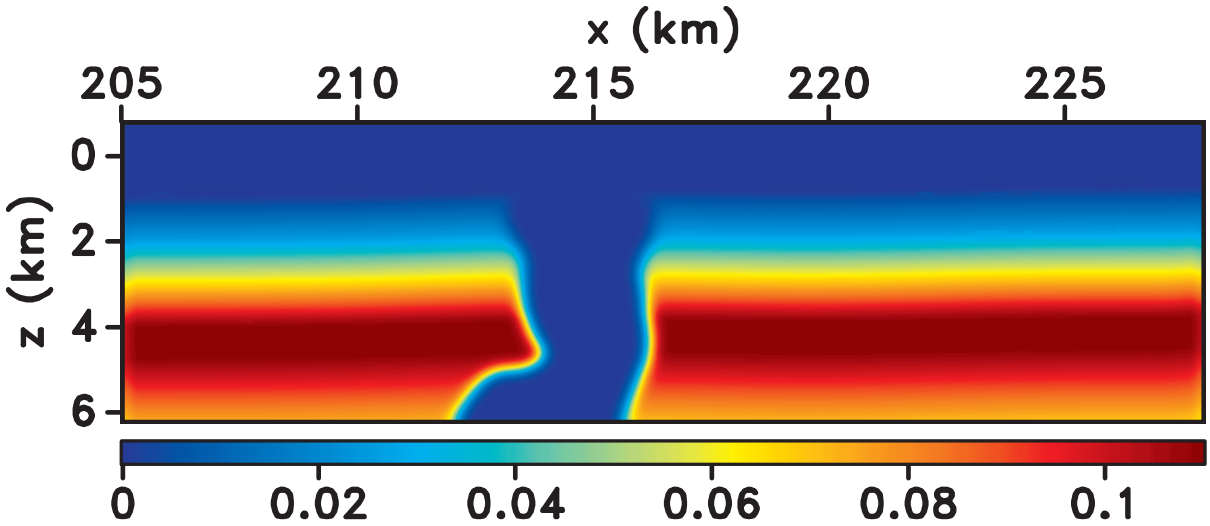

(b)

Figure 13. Initial elliptic ($\eta = 0$) model for the line from the Gulf of Mexico: (a) $V_{\rm nmo}$ (with mirror geometry used for imaging and tomography) and (b) $\delta = \epsilon$.

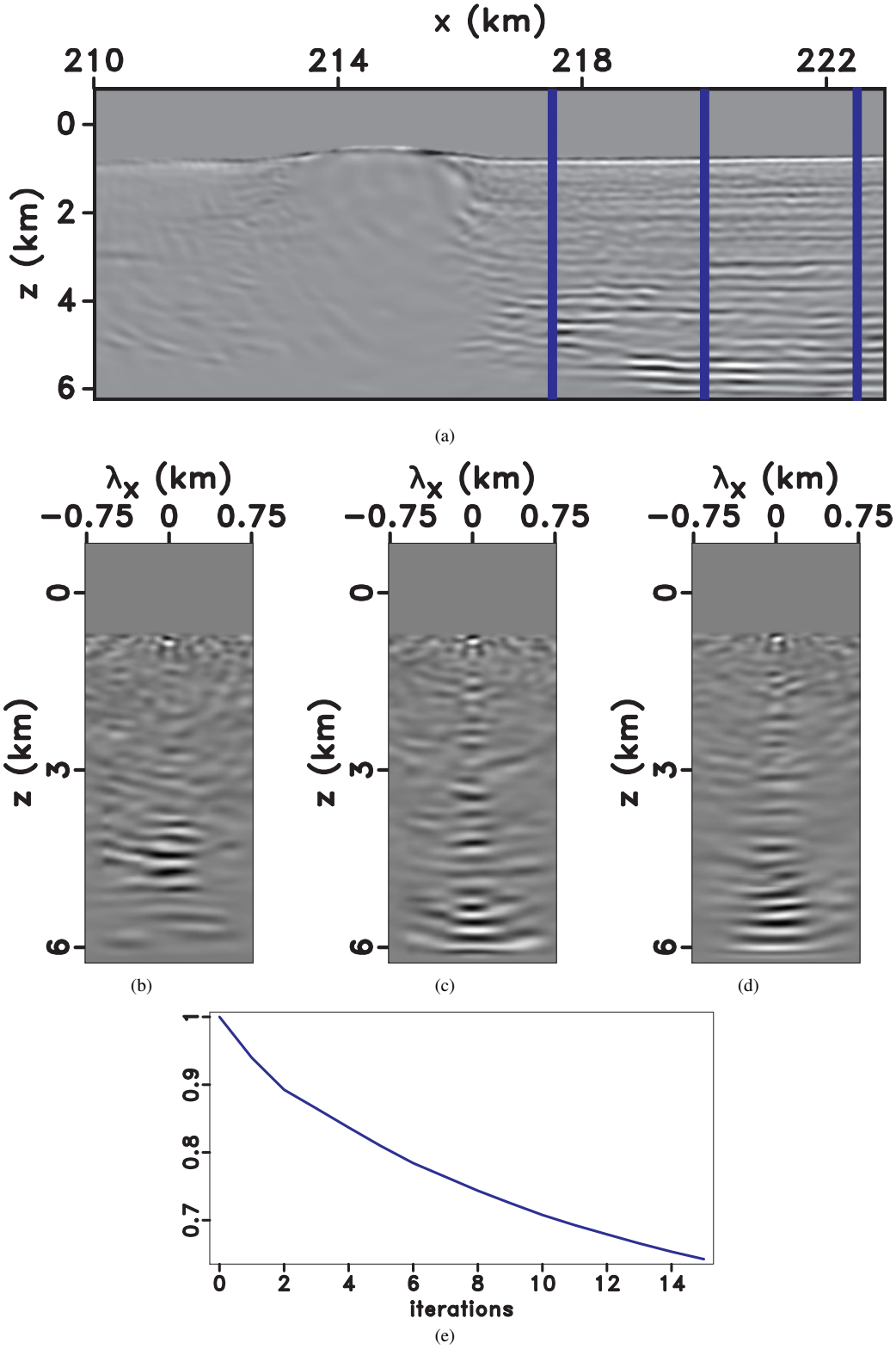

Figure 14. LSRTM output for the model from Figure 13. (a) The conventional image and (b-d) the space-lag gathers at the locations marked by the vertical blue lines. (e) The normalized LSRTM objective function.

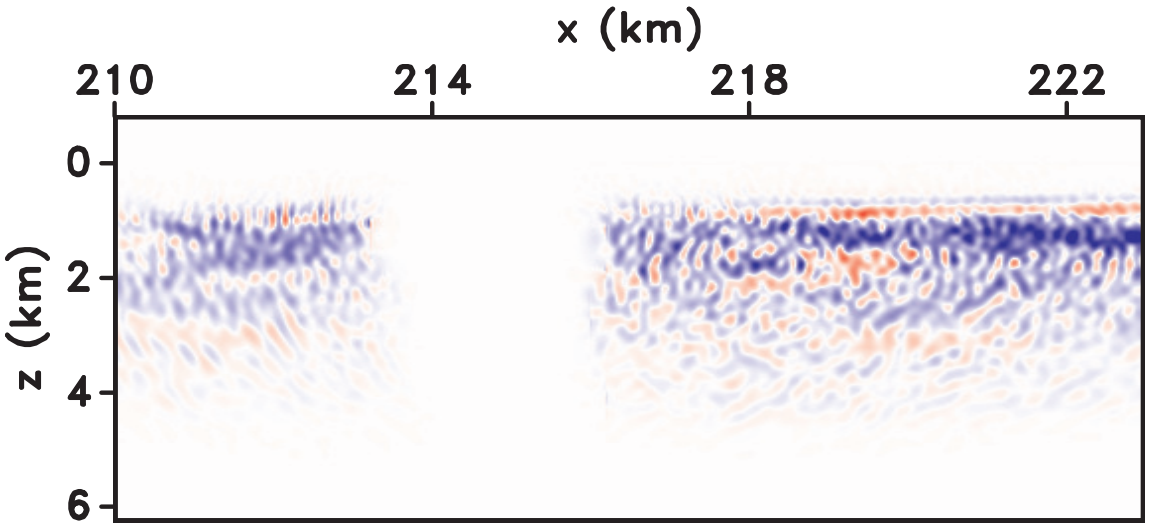

(a)

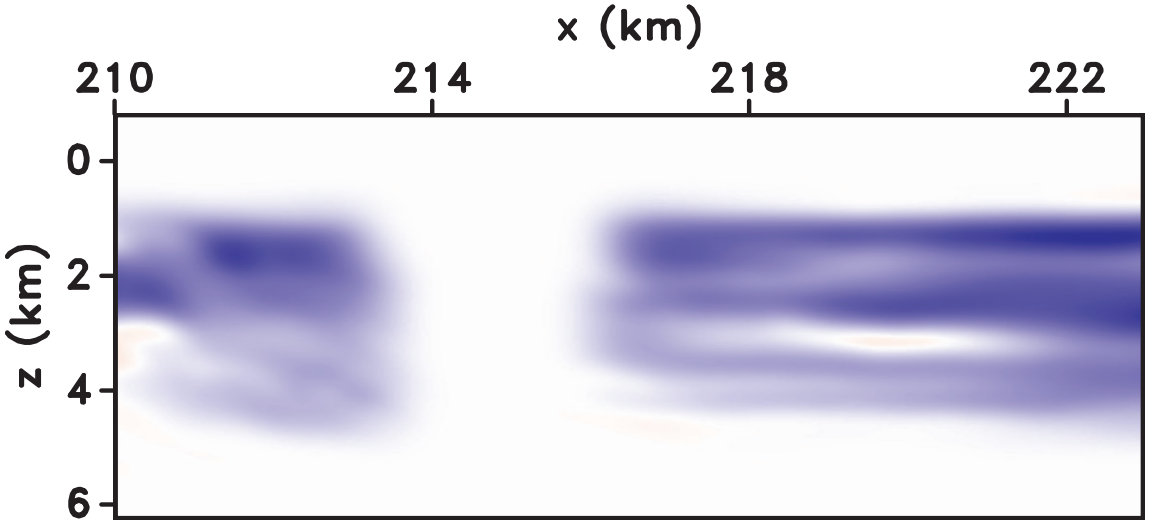

(b)

Figure 15. IDT gradient for η (a) before and (b) after preconditioning.